ELSEVIER

Contents lists available at ScienceDirect

Chemical Engineering Journal

journal homepage: www.elsevier.com/locate/cej





Upcycling wastewater nitrate into ammonia fertilizer via concurrent electrocatalysis and membrane extraction

Ning Shi ^{a,1,2}, Jianan Gao ^{b,1,3}, Kai Li ^{a,4}, Yifan Li ^{a,5}, Wen Zhang ^{b,6}, Qipeng Yang ^{a,7}, Bo Jiang ^{a,*,8}

- ^a School of Environmental and Municipal Engineering, Qingdao University of Technology, Qingdao 266033, PR China
- b John A. Reif, Jr. Department of Civil and Environmental Engineering, New Jersey Institute of Technology, Newark, NJ 07102, the United States

ARTICLE INFO

Keywords: Electrocatalysis FeNi catalyst Nitrate reduction Membrane extraction Ammonia recovery

ABSTRACT

Electrocatalytic upcycling of nitrate (NO₃) in wastewater into the valuable ammonium-based fertilizer has been considered as a green and appealing alternative to biological nitrogen removal or the industrial ammonia (NH3) production processes. This work investigated an innovative and energy-efficient electrolysis flow-through cell consisting of a porous activated iron nickel (FeNi) alloy cathode and a hollow polypropylene fiber membrane extraction unit to realize the electrochemical NO₃ reduction and simultaneous upcycling to ammonium sulphate salts ((NH₄)₂SO₄). Cathodic and anodic electrochemical half-reactions were coupled to enable NO₃ reduction to ammonia and in-situ acid/base productions to promote the membrane stripping of NH3. Our results show that after electrolysis operation for 14 h for a synthetic wastewater containing 150 mM NO₃ under a cathodic current density of 30 mA·cm⁻², 99 % of NO₃ removal efficiency, 98 % of ammonia selectivity, 93 % of Faradic efficiency and 97 % of total ammonia nitrogen (TAN) recovery were achieved respectively. A NH3 recovery flux and a specific energy consumption reached 2050 g-(NH₄)₂SO₄·m⁻²·d⁻¹ and 11 kWh·kg⁻¹-(NH₄)₂SO₄, respectively, which outcompetes many reported processes. Direct electron transfer was the main mechanisms of electrochemical NO₃ reduction to ammonia. Interfacial reaction thermodynamics and kinetics analysis of key intermediates (e.g., *NO₃, *NO₂, and *NO) shows that the NiFe₂O₄ (3 1 1)-Ni site on the thermally activated FeNi alloy surface exhibited higher reactivity and specificity toward electrochemical NO₃ reduction to ammonia over nitrogen (N2) or hydrogen (H2) generation. Ultimately, this study aims to promote sustainable nitrogen nutrient recovery and ammonia fertilizer synthesis from wastewater treatment.

1. Introduction

The industrial production of ammonium fertilizers mainly relies on the Haber-Bosch process [1], which involves the thermodynamically unfavorable reactions between nitrogen (N₂) and hydrogen (H₂) at high temperatures (350–550 °C) and pressures (15–25 MPa) [2]. To react with N₂, 941 kJ·mol $^{-1}$ is needed to break the N $\!\equiv$ N bond. By contrast,

nitrate (NO_3^-) could be disintegrated into deoxygenated species with a much lower energy of $204 \, kJ \cdot mol^{-1}$ [3]. Meanwhile, diverse wastewater from photovoltaic, semiconductor manufacturing, and nuclear fuel processing industries provides abundant sources of NO_3^- (e.g., 4–20 g-nitrogen- L^{-1}) that could threat the ecological safety and human health if not properly treated [4]. Therefore, it is critical to develop effective technologies to recover this important nutrient source and convert it

E-mail address: bjiang86upc@163.com (B. Jiang).

- The author contributed equally to this work.
- ² Ning Shi: 0000-0001-6204-0639.
- ³ Jianan Gao: 0000-0003-1255-1240.
- ⁴ Kai Li: 0000-0003-0329-3649.
- ⁵ Yifan Li: 0000-0003-0329-3649.
- $^{\rm 6}$ Wen Zhang: 0000-0001-8413-0598.
- ⁷ Qipeng Yang: 0000-0003-4725-1491.
- ⁸ Bo jiang: 0000-0001-9500-2145.

^{*} Corresponding author.

into valuable products.

Direct electrocatalytic NO₃ reduction into ammonia (NH₃) or ammonium (NH₄⁺) has proven promising for addressing the above nitrate pollution and sustainable nitrogen resource recovery. Over the past few years, non-metallic carbon-based materials, monometallic based materials (including precious metals such as Pd, Pt, Rh, Ru, Ir and transition metals such as Cu, In, Sn, Fe, Ni, Ti, Co), and bimetallic based materials have been widely studied toward the electrocatalytic reduction NO₃ into NH₄ in the literature [5]. Among these, the bimetallic electrocatalysts that combine the benefits of different metals exhibit high catalytic activity and product selectivity. For example, CuNi alloy catalysts were demonstrated for the electrochemical reduction of NO_3^- to ammonia with a high Faradaic efficiency of 99 %, because of Ni alloying can tune the adsorption energies of intermediates such as *NO3 and *NO₂ for promoting the reduction of NO₃ [6]. However, the complicate and costly catalyst preparation for Cu based alloy catalysts has hindered their practical applications. Inserted, Fe based electrocatalyst are emerging as effective and economical options for denitrification due to its unique advantages (e.g., cheap and easy to obtain, non-toxic and harmless) [7]. But the reaction activities need to be further improved since the formations of stable intermediates (*NO₃, *NO₂, and *NO) for electrochemical NO₃ reduction to ammonia or N₂ are the rate-limiting steps in the entire reaction for Fe catalysts due to the difficulty of breaking N-O [7]. In addition, the electrolytic conversion of NO₃ to ammonia is limited by the mass transfer of NO₃ from the bulk solution toward the cathode surface and the accumulation of gaseous products (e. g., NH₃, N₂, H₂ and N₂O) on the cathode surface [8]. Specifically, the gas bubbles such as H2 and NH3 generated on the electrode surface may reduce the electrocatalytic active area, block ion transport channels, and cause current drop due to a bubble layer formation between the cathode and the electrolyte. Thus, effective stripping or abstraction of NH3 may be an effective strategy to improve the efficiency of electrochemical reduction of NO₃ to ammonia.

There is a limited number of studies that reported the electrochemical nitrate reduction in combination with ammonia recovery. For example, most common approaches such as air stripping [9], liquid-gas membrane [10], electrodialysis [11], and struvite precipitation [12] only complete NH3 extraction or stripping and are unable to produce ammonia from the NO₃ containing wastewater. Likewise, many electrochemical studies just demonstrated the electrochemical reduction of NO₃ to ammonia without recovering the produced ammonia [13–15]. Therefore, the produced ammonia still remaining in the water would certainly lead to the secondary pollution of water bodies. In our previous study [16], we used a CuO@Cu foam and a flat-sheet polytetrafluoroethylene membrane for reducing NO₃ to ammonia and upcycling NH₃ into (NH₄)₂SO₄. However, this system showed a low Faraday efficiency (15-55 %) and a low NH_4^+ selectivity (78.7-85.1 %) with a total ammonia nitrogen (TAN) recovery of only 78.6 %-85 % and high energy consumption (21.8-33.5 kWh·kg⁻¹-(NH₄)₂SO₄), probably because of the strong competitive hydrogen evolution reaction and interfacial mass transfer on the three-phase cathodic membrane. Besides, the NH3 production flux (436 g-N·m $^{-2}$ ·d $^{-1}$) was much faster than the NH $_3$ recovery flux (220 g-N·m⁻²·d⁻¹), which resulted in the ammonia accumulation and an extended operation time of 3 h required to strip the produced NH_3 (even with the additional used of an aeration pump) after the electrochemical nitrate reduction reaction ended.

In this study, we integrated a flow-through electrolysis cell using a bimetallic iron nickel (FeNi) alloy as the cathode catalyst and a separate hollow membrane device for NH $_3$ extraction. This decoupling of the electrochemical nitrate reduction and NH $_3$ stripping was demonstrated to significantly improve the two processes compared to the two coupled processes on the gas-permeable cathode membrane. The effects of operation parameters (e.g., current density) and water matrices (NO $_3^-$ and Cl $_2^-$ concentrations) on electrochemical NO $_3^-$ reduction and NH $_3$ recovery were all investigated. Based on the density functional theory (DFT) and scavenging experiments, the activity and mechanisms of

electrolytic NO_3^- reduction to ammonia at the activated FeNi alloy cathode was revealed. Finally, the performance of NO_3^- removal and NH_3 recovery from real wastewater was also assessed to provide new insights into the practical applications.

2. Materials and methods

2.1. Activated FeNi cathodic catalyst preparation

The bimetallic FeNi foam electrode (4 cm \times 4 cm, purity >99.9 %, a pore density of 95 pores per linear inch or ppi, a pore size of 0.26 mm, and a thickness of 1 mm) was purchased from Kunshan Lvchuang Electronic Technology Co., Ltd. (China). The FeNi foam was thermally calcinated at 400 °C for 1 h at a heating rate of 5 °C min⁻¹ under a pure oxygen atmosphere to activate the FeNi cathode by forming a FeNi oxide layer [17]. After calcination, the obtained FeNi cathode was stored in vacuum for future use. Other used chemicals are described in detail in the section S1 of the supporting information (SI).

2.2. Material Characterization, chemical analysis, and electrochemical tests

The structure and morphology of the cathode catalysts were characterized by scanning electron microscope (SEM), transmission electron microscope (TEM) and energy dispersive X-ray spectroscopy mapping (EDS-mapping). X-ray diffraction (XRD) patterns were collected using a Bruker D2 PHASER X-ray diffractometer within 20 angle range of 10° -80°. The valence state and bonding structure of the elements were determined by X-ray photoelectron spectroscopy (XPS, Thermo Fisher ESCALAB 400Xi spectrometer with Al K α radiation). The quantity of Fe and Ni leached into the solution were analyzed by ICP-AES (ICP2060t, Tianrui Co., China).

All electrochemical tests of catalysts were carried out in a typical Htype reactor as illustrated in Fig. S1 in the section S2. The treated FeNi bimetallic foam (1 cm × 1 cm), a saturated calomel electrode (SCE, +0.241 V vs SHE), and a platinum foil (1 cm \times 1 cm) were used as the working electrode, the reference electrode, and the counter electrode, respectively. According to the Nernst equation ($E_{RHE} = E_{Ag/AgCl} + 0.059$ pH + 0.197 V), all the potentials were converted into the potential of the RHE. The cathode and anode chambers were separated by a proton exchange membrane (PEM, Dupont, Nafion 117). Linear sweep voltammetry (LSV), cyclic voltammetry (CV), and electrochemical impedance spectroscopy (EIS) tests were performed on a CHI660E electrochemical workstation (Chenhua Instrument Co., Ltd.; Shanghai; China). LSV polarization curves with/without NO₃ in the electrolyte were performed at a scan rate of 100 mV·s⁻¹. To obtain the electrochemical double-layer capacity (EDLC, Cdl), CV tests were conducted at a rate (v) of $10-50 \text{ mV}\cdot\text{s}^{-1}$, which was recorded at a potential step of 0.1 V near the open-circuit potential (OCP) to avoid faradaic processes [18,19]. The C_{dl} value was calculated based on Eq. (1) according to the response current values (Ia and Ic) and the scan rate. EIS analysis of the pristine and thermally activated FeNi foam were conducted at the OCP from -0.1 and -0.3 V/RHE, respectively, under the alternating current within the frequency range from 10^5 to 10^{-2} Hz at an incremental change of 5 mV in a electrolyte containing 5.0 mM K₃Fe(CN)₆ and 5.0 mM K₄Fe(CN)₆.

$$\frac{I_a - I_c}{2} = C_{dl}v\tag{1}$$

2.3. Structure design and working principle of the continuous flow-through electrolysis cell

Fig. 1a illustrates the conceptual design of this continuous flow-through electrolysis cell integrating electrocatalytic NO₃ reduction with concurrent NH₃ recovery. Briefly, a titanium/ iridium oxide-

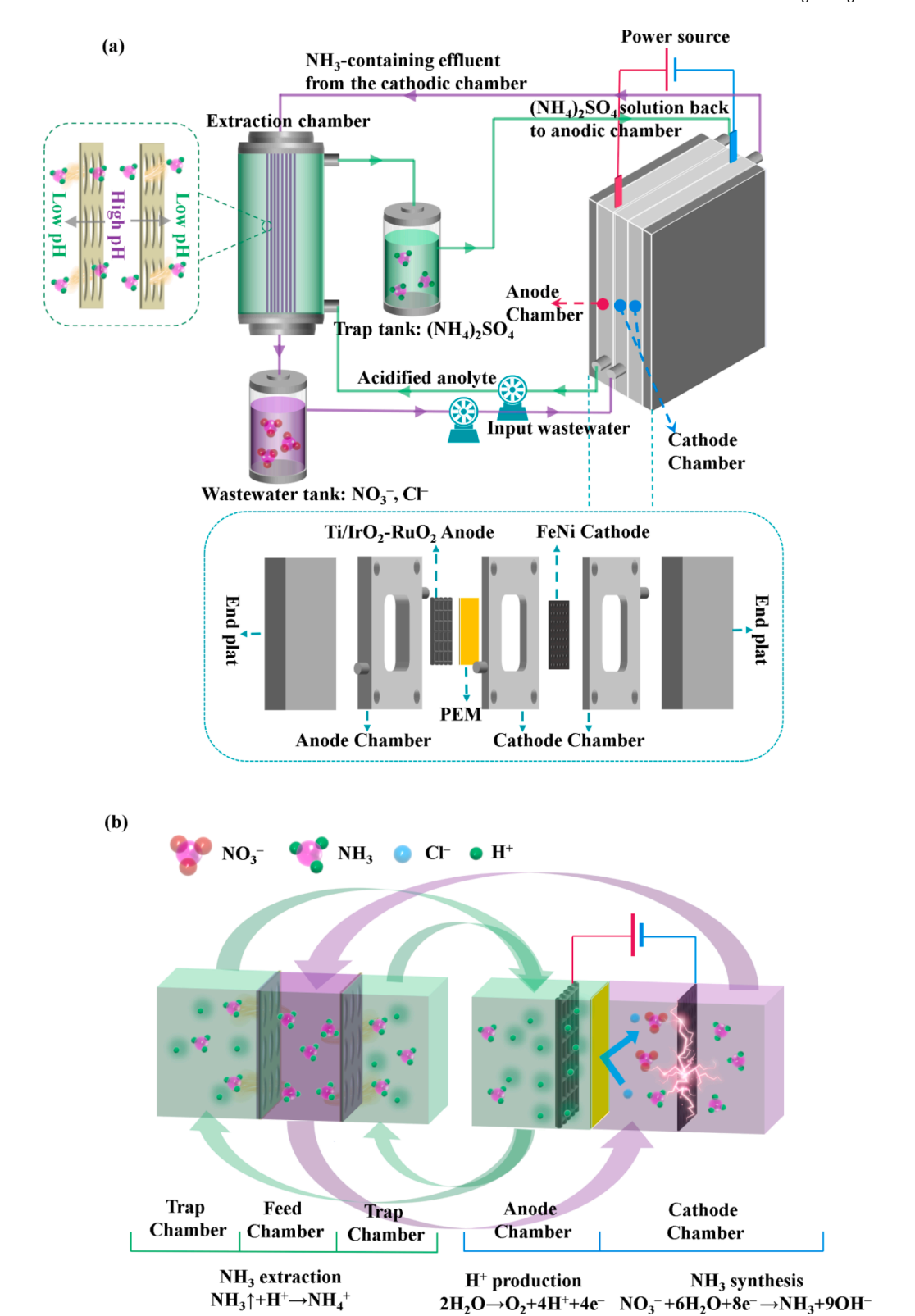


Fig. 1. The schematic of the employed flow-through electrolysis cell and its operation principle. A photo of this benchtop setup with detailed annotation is provided in Fig. S2.

ruthenium oxide (Ti/IrO $_2$ -RuO $_2$) plate (4 cm \times 4 cm) was purchased from Yunxuan Metallic Materials Co. Ltd and used as the anode, which was shown not to cause the direct oxidation of NH $_4^+$ [20]. The FeNi foam was used as the cathode and placed 6 mm away from the Ti/IrO $_2$ -RuO $_2$ anode. The cathode and anode chambers were separated by the same

nafion PEM to prevent the diffusion of the active chlorine (HOCl or OCl $^-$) from the anodic chamber into the cathode chamber, which could oxidize NH $_4^+$ /NH $_3$ into N $_2$ [21]. The synthetic NO $_3^-$ wastewater or real wastewater was pumped into the one of the two cathode chambers at a flow rate of 100 mL·min $^{-1}$ and forced to pass through the porous FeNi

foam and enter the other chamber. The cathodic reactions (annotated in Fig. 1b) led to electrochemical reduction of NO_3^- and a high solution pH in the range of $12.0{\text -}14.0$ that promoted the vaporization of NH_3 . The alkaline effluent from the cathodic chamber was pumped into the inner hollow fiber membrane (Hangzhou Xinhui Membrane Technology Co., Ltd, China) with a total membrane surface area of $1.5~\text{m}^2$ to strip NH_3 . Meanwhile, an anolyte $(0.1~\text{M Na}_2SO_4)$ in the trap tank was pumped into the anode chamber at a flow rate of $100~\text{mL}{\cdot}\text{min}^{-1}$ and was acidified at the anode via the H_2O -splitting reaction (Fig. 1b). Then, the acidic anolyte was pumped into the outer chamber of the hollow fiber membrane module to drive the membrane stripping of NH_3 from the inner fluid. The arrested NH_3 in the trap solution was finally circulated back into the trap tank.

2.4. Evaluations of the nitrate reduction and ammonia recovery

2.4.1. Analysis of the mass transfer rate constant

To characterize the mass transfer for the pristine and activated FeNi cathodes, the limiting current (I_{lim}) was measured by placing those cathodes in a electrolyte containing 5 mM K_4 Fe(CN)₆, 5 mM K_3 Fe(CN)₆, and 0.1 M N_2 SO₄ as the background electrolyte. Then, the mass transfer rate constant (k_m) was calculated based on the Eq. (2) [22]:

$$k_m = \frac{I_{\text{lim}}}{z \times F \times A \times C_b} \tag{2}$$

where z is the number of electrons transferred (1), F is the Faraday constant (96,485C·mol $^{-1}$), A is the geometric surface area of the electrode (m 2), and C_b is the bulk concentration of Fe(CN) $_6^{3-}$ (mol·m $^{-3}$), and I_{lim} for activated FeNi and pristine FeNi is 0.12A and 0.04A, respectively.

2.4.2. Determination of the nitrate removal efficiencies, rates, and reaction selectivity

Water samples in wastewater and trap tanks were collected and filtered through 0.45- μ m cellulose membranes (Millipore) to monitor different nitrogen species (e.g., ammonia and nitrate). The detailed measurement methods are provided in the section S3. The calculations of NO $_3$ removal efficiency (R_{NO_3}) R_{NO_3} -N, NO $_2$ selectivity (S_{NO_2}) S_{NO_2} -N, N $_2$ selectivity (S_{N_2}), total ammonia nitrogen (TAN) selectivity (S_{TAN}), and total ammonia nitrogen (TAN) recovery efficiency were calculated by Eq. (S1)-(S7).

2.4.3. Evaluation of the energy efficiency for electrochemical nitrate reduction and ammonia production

The Faradic efficiency (FE) (%) for NH $_{\!3},\ N_2,\ and\ NO_2^-$ were all calculated by Eq. (3):

$$FE(\%) = \frac{n \times F \times N_i}{Q} \times 100 \tag{3}$$

where n is the amount (mol) of the produced NH₃, N₂, or NO $_2$, F is the Faraday constant, N_i is the electron transfer number per more of reduced nitrate and is equal to 8, 5, and 2 if nitrate is reduced to NH₃, N₂, and NO $_2$, respectively, Q is the total charge (C) passing the electrode, which was calculated based on the integration of the current curve I (A) vs t (s).

The specific energy consumption (EC) $(kWh\cdot kg^{-1}-(NH_4)_2SO_4)$ was calculated by Eq. (4) to evaluate the energy cost for the produced ammonia product:

$$EC = 10^{-3} \times E_{cell} \times I \times t \times m^{-1}$$
(4)

where E_{cell} is the total cell potential (V), $I \times t$ is the integral area under the curve I vs t (A·h), and m is the mass of the produced (NH₄)₂SO₄ (kg).

2.5. DFT calculations

The DFT calculations were conducted using the Vienna ab initio Simulation Package (VASP) to determine the electron distribution, active sites, and the energy barriers of reaction determining steps for the activated FeNi cathode toward the NO_3^- reduction. According to the analysis of the dominant lattice planes in XRD, the (3 1 1) facet of NiFe₂O₄ was selected as the studied reaction interface for DFT calculation. Additionally, the pure metal surfaces such as Ni (1 1 1) and Fe (1 1 0) were reported previously [4,23] and applied as control subjects in this work. Detailed information about the DFT/VASP operations is provided in section S5.

3. Results and discussions

3.1. Morphology, element mapping, crystallinity and surface chemical states of the FeNi foam cathode

The surface structure and surface chemistry of the porous FeNi foam before and after the calcination treatment at 400 °C are compared. Fig. 2 shows the pristine FeNi foam turned to slightly black after calcination and numerous needle-like structures or nanowire arrays formed on the surface. The formation of this microstructures or nanowire arrays could result from the surface oxidation reactions and formation of a metal oxide layer. This rough surface structure gives rise to the active sites for mass transfer and reactions compared to the pristine foam surface [24].

Fig. S3a, b shows the chemical element mapping on the pristine and thermally activated FeNi foams. Three major elements, Fe, Ni and O, are identified for both samples. The EDS mapping of the Fig. S3c further shows the pristine FeNi foam had an atomic percentage of 66at%, 24at %, and 10at%, respectively for Fe, Ni, and O elements that agrees with the previous study [25]. However, the O elements increased to 48at% on the activated FeNi surface, owing to the formation of FeNi oxides after calcination [26].

The XRD patterns in Fig. S3d show that the pristine FeNi foam yielded two peaks at 44.6° and 64.9°, which implies the presence of the Kamacite form (JCPDS No. 37-0474) [27]. The other two peaks at 43.5° and 50.7° may correspond to Taenite (JCPDS No. 47-1417) [27]. After calcination, the peak intensities at 44.6° and 64.9° for Kamacite (JCPDS No. 37-0474) decreased and some new peaks at 35.8° , 43.4° , and 62.9° involved, which correspond to the (3 1 1), (4 0 0), and (4 4 0) lattice planes of NiFe₂O₄ (JCPDS no.74-2081), respectively [28,29] and suggests the formation of mixed FeNi oxide formation on the activated FeNi foam surface. High resolution TEM (HRTEM) image of the activated FeNi was shown in Fig. S4a, where the primarily exposed crystal planes of NiFe₂O₄ were (3 1 1) with the lattice spacing (d) of 0.25 nm [30]. Selected-area electron diffraction (SAED) clearly presents continuous ring patterns that can be ascribed to the (3 1 1), (4 0 0), and (4 4 0) planes of the NiFe₂O₄ (Fig. S4b), which were consistent with the XRD patterns.

Fig. S5 shows the XPS spectra that reveal the changes of the surface chemical compositions and valence states of the FeNi composite. In the high-resolution Fe 2p spectrum of the pristine FeNi foam, three distinct peaks at binding energies of 707 eV, 710.0 eV, and 712 eV were attributed to Fe⁰, Fe²⁺, and Fe³⁺, respectively [31,32]. In contrast, no Fe⁰ was detected in the activated FeNi foam after calcination and the proportion of $\mathrm{Fe^{3+}}$ increased from 70 % to 84 %. This is attributed to the acquisition of lattice oxygen in the alloy, which may change the valence state of Fe from low to high [33]. The peaks at 852.6 eV and 856.0 eV for the Ni 2p spectrum corresponded to Ni⁰ and Ni²⁺ and the peak at 861.4 eV corresponded to satellite peak of Ni²⁺ [34,35]. The peak strength of Ni^{2+} increased from 63 % to near 100 % after thermal calcination. This result can be explained by the fact that the Ni element in the alloy phase overcome the thermodynamic limitations for the formation of Ni oxides probably due to the Fe-Ni synergistic effects and transforms to Ni²⁺, resulting the formation of the NiFe₂O₄ phase with spinel structure [32].

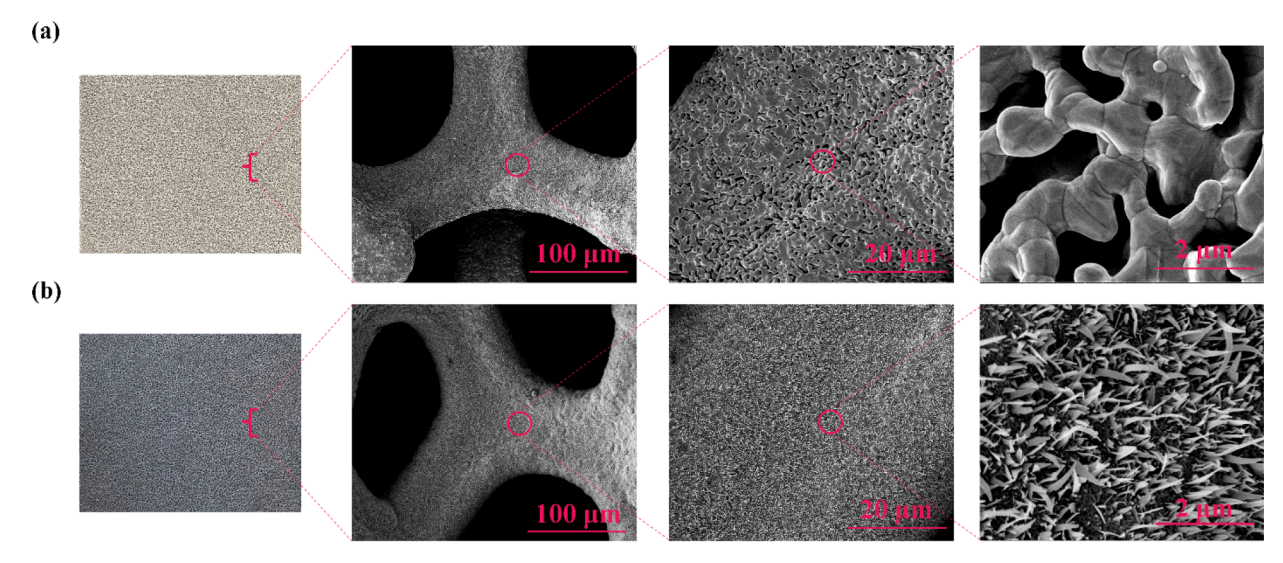


Fig. 2. Photos and SEM images of the pristine (a) and (b) thermally activated FeNi cathode or foam.

The XPS results support the EDS mapping and XRD results that indicate a mixed FeNi oxide layer formed on the activated FeNi foam surface.

3.2. Electrochemical characterization

The LSV curves in Fig. 3a compares the response currents using different materials as cathodes, which shows the activated FeNi cathode had a relatively high overpotential for H₂ evolution reaction (HER) with an onset potential of -0.70 V/RHE in Na₂SO₄ without NO₃, whereas in the presence of 20 mM NO_3^- , the onset potential increased to -0.19 V/RHE, which is more positive than those of the pristine FeNi cathode (-0.33 V/RHE), the pure Fe foam cathode (-0.36 V/RHE), and the pure Ni foam cathode (-0.88 V/RHE). This suggests a higher cathodic reactivity for the activated FeNi cathode toward NO₃ reduction reaction than other three materials. In addition, among these cathode materials, the activated FeNi cathode had a faster current growth rate with the decreasing cathode potential. The response currents (Ia and Ib) under different scan rates were recorded in the CV spectra, which was mainly caused by adsorption and desorption of nitrate at the active site and the charging and discharging of the electric double layer (Fig. S6a, b and Table S1) [18]. At the same scan rate, the charging currents of the activated FeNi are bigger than that of pristine FeNi, indicating activated FeNi have bigger accessible active area than that of pristine FeNi. The electrochemical double-layer capacitance (C_{dl}) was determined by Eq. (1) and equal to 5.8 mF·cm⁻² and 10.1 mF·cm⁻², respectively for the pristine FeNi cathode and the activated FeNi cathode in Fig. 3b. It is known that the electrochemically active surface area is proportional to

the value of C_{dl} [18]. Clearly, the activated FeNi cathode rendered a greater number of electrochemically active surface area for NO_3^- reduction than the pristine FeNi cathode. Furthermore, the current–time curves of activated FeNi under different polarization potentials are recorded. As shown in Fig. S7, the activated FeNi exhibited poor HER catalytic activity within these polarization potential ranges. The potentiostatic polarization curve remained stable after a short charge and discharge of the electric double layer, indicating that activated FeNi has continuous and stable catalytic activity.

The Nyquist plots and the corresponding equivalent circuits in Fig. 3c show that the interfacial impedance of the pristine FeNi and activated FeNi solids both consisted of an electrolyte resistance (R₁) and the charge transport resistances (Rct) [36]. Table S2 summarizes the results of R₁, R_{ct} and C_{dl}. The pristine FeNi cathode and the activated FeNi cathodes had similar R₁ with the value of $20.2 \,\Omega \cdot \text{cm}^{-2}$ and $19.5 \,\Omega \cdot \text{cm}^{-2}$, respectively. However, the activated FeNi cathode exhibited lower R_{ct} value (49.8 $\Omega \cdot \text{cm}^{-2}$) than the pristine FeNi cathode (183.9 $\Omega \cdot \text{cm}^{-2}$), largely because of the surface formation of the nanowire arrays that could facilitate the mass and electron transport from/to the cathode surface [20]. For example, based on the measurements of the limiting current (I_{lim}) on the pristine and activated FeNi cathode, the mass transfer rate constant (k_m) was calculated by Eq. (2) and was found higher $(1.55 \times 10^{-1} \text{ m} \cdot \text{s}^{-1})$ than that $(5.46 \times 10^{-2} \text{ m} \cdot \text{s}^{-1})$ of the pristine FeNi in the flow-through mode. In addition, the C_{dl} value was recalculated by the capacitance at electrode-electrolyte interface (CPE) in the EIS equivalent circuit fitting [37], which yielded 11.0 mF·cm⁻² and 5.1 $\mathrm{mF}{\cdot}\mathrm{cm}^{-2}$ for the activated FeNi cathode and the pristine FeNi

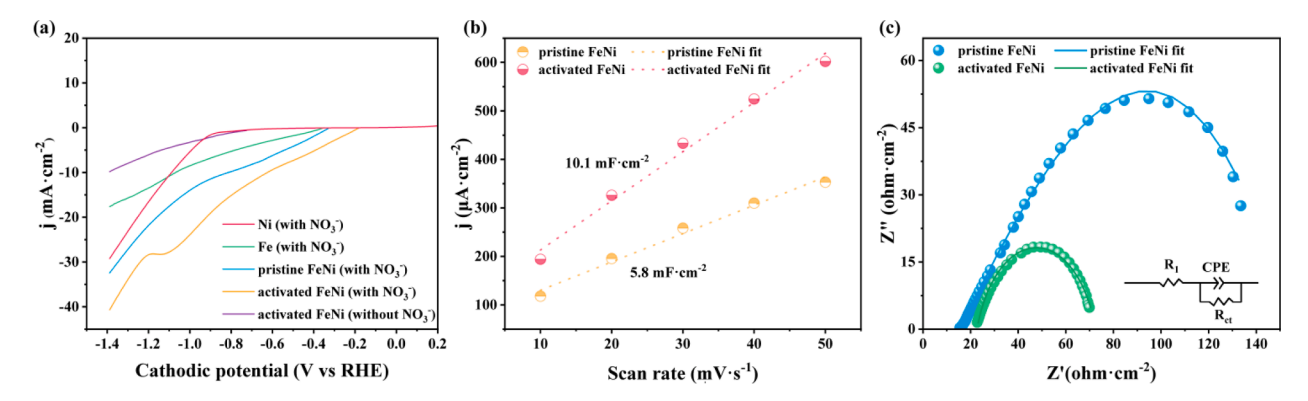


Fig. 3. (a) LSV curves of various cathode materials. (b) The plots of response current values (I_a and I_c) as a function of the scan rate for the pristine FeNi cathode and activated FeNi cathode. (c) Nyquist plots of the pristine and activated FeNi cathode.

cathode, respectively, and agreed well with the $C_{\rm dl}$ values calculated from the CV test. Clearly, the activated FeNi cathode exhibited a relatively high electrolytic activity, a large electrochemically active surface area, and a high interfacial electron transfer efficiency for the electrocatalytic NO_3^- reduction.

3.3. Electrocatalytic NO₃ reduction performance

Fig. 4a shows that the NO_3^- reduction efficiency was near $\sim 100 \%$ at the activated FeNi foam cathode after 2.5 h of the operation with major experimental conditions detailed in the caption. By contrast, only 88 %, 72 % and 5 % were achieved for the pristine FeNi, Fe, and Ni foam cathodes, respectively. Accordingly, Fig. S8 shows that the activated FeNi cathode had the highest Faradic efficiency for nitrate reduction (72 %), followed by the Fe (52 %), Ni (4 %) and pristine FeNi (63 %) cathodes. And the Faradic efficiency for HER by the activated FeNi cathode reached 28 %, lesser than those of the pristine FeNi cathode (37 %), Fe (48 %) and Ni (96 %). The pseudo-first-order rate constant for electrochemical nitrate reduction reaction follow the order of Ni (3.990 $\times 10^{-4} \, \mathrm{min^{-1}}) < \mathrm{Fe} \, (7.97 \times 10^{-3} \, \mathrm{min^{-1}}) < \mathrm{pristine} \, \mathrm{FeNi} \, (1.043 \times 10^{-2} \, \mathrm{min^{-1}}) < \mathrm{pristine} \, \mathrm{FeNi} \, (1.043 \times 10^{-2} \, \mathrm{min^{-1}}) < \mathrm{pristine} \, \mathrm{FeNi} \, (1.043 \times 10^{-2} \, \mathrm{min^{-1}}) < \mathrm{pristine} \, \mathrm{FeNi} \, (1.043 \times 10^{-2} \, \mathrm{min^{-1}}) < \mathrm{pristine} \, \mathrm{FeNi} \, (1.043 \times 10^{-2} \, \mathrm{min^{-1}}) < \mathrm{pristine} \, \mathrm{FeNi} \, (1.043 \times 10^{-2} \, \mathrm{min^{-1}}) < \mathrm{pristine} \, \mathrm{FeNi} \, (1.043 \times 10^{-2} \, \mathrm{min^{-1}}) < \mathrm{pristine} \, \mathrm{FeNi} \, (1.043 \times 10^{-2} \, \mathrm{min^{-1}}) < \mathrm{pristine} \, \mathrm{FeNi} \, (1.043 \times 10^{-2} \, \mathrm{min^{-1}}) < \mathrm{pristine} \, \mathrm{FeNi} \, (1.043 \times 10^{-2} \, \mathrm{min^{-1}}) < \mathrm{pristine} \, \mathrm{FeNi} \, (1.043 \times 10^{-2} \, \mathrm{min^{-1}}) < \mathrm{pristine} \, \mathrm{FeNi} \, (1.043 \times 10^{-2} \, \mathrm{min^{-1}}) < \mathrm{pristine} \, \mathrm{FeNi} \, (1.043 \times 10^{-2} \, \mathrm{min^{-1}}) < \mathrm{pristine} \, \mathrm{FeNi} \, (1.043 \times 10^{-2} \, \mathrm{min^{-1}}) < \mathrm{pristine} \, \mathrm{FeNi} \, (1.043 \times 10^{-2} \, \mathrm{min^{-1}}) < \mathrm{pristine} \, \mathrm{FeNi} \, (1.043 \times 10^{-2} \, \mathrm{min^{-1}}) < \mathrm{pristine} \, \mathrm{FeNi} \, (1.043 \times 10^{-2} \, \mathrm{min^{-1}}) < \mathrm{pristine} \, \mathrm{FeNi} \, (1.043 \times 10^{-2} \, \mathrm{min^{-1}}) < \mathrm{pristine} \, \mathrm{FeNi} \, (1.043 \times 10^{-2} \, \mathrm{min^{-1}}) < \mathrm{pristine} \, \mathrm{FeNi} \, (1.043 \times 10^{-2} \, \mathrm{min^{-1}}) < \mathrm{pristine} \, \mathrm{FeNi} \, (1.043 \times 10^{-2} \, \mathrm{min^{-1}}) < \mathrm{pristine} \, \mathrm{$ min^{-1}) < activated FeNi (1.849 \times 10⁻² min^{-1}) [38]. Finally, we also confirmed that no NO_3^- was removed within 2.5 h under the open circuit condition or when no cathodic potential was applied, indicating that the direct reduction of NO₃ by the FeNi alloy foam was negligible.

Fig. S9 compares the TAN and NO_2^- concentrations in different cathodic flow-cells under the different operation time. Except the Ni cathode, all the other three cathodes produced TAN, NO_2^- and some minor N_2 . The NO_2^- concentration first accumulated and then started to

reduce. The activated FeNi cathode completely removed NO_2^- after 2.5 h, whereas the Fe, pristine FeNi and Ni cathodes yielded a residual NO_2^- concentration of approximately 0.9 mM, 0.5 mM, and 0.2 mM respectively. Noticeably, the produced TAN concentration by the activated FeNi cathode reached 19.6 mM, greater than those of the pristine FeNi cathode (15.9 mM), Fe (13.8 mM) and Ni (0.6 mM). The possibility of the generation of ammonia from the dissolved N_2 from the air transfer is excluded, as no ammonia was detected after 2.5 h in the Na_2SO_4 electrolyte. Moreover, the electrochemical N_2 production was also minimum for the activated FeNi cathode, whereas for the pristine FeNi and Fe cathodes, the N_2 production was evident. Accordingly, the activated FeNi cathode achieved the highest TAN selectivity (98 %), followed by the Fe (84 %), Ni (54 %) and pristine FeNi (91 %) cathodes.

The stability of the NO_3^- reduction on the activated FeNi cathode was also evaluated. Fig. 4b shows the NO_3^- removal efficiency and TAN selectivity for the activated FeNi cathode remained relatively stable at near 100 % and 98 %, respectively, in 20 consecutive operation recycles (2.5 h per cycle). At the end of the first recycle, only 0.0220 mg·L $^{-1}$ Fe and 0.0034 mg·L $^{-1}$ Ni were leached into the solution, but the metal ion release became less significant in the following recycles and was hardly detected after four recycles. To examine the chemical state changes, XPS analysis was conducted on the used FeNi cathode. Fig. S10a, b revealed an obvious increase in the oxygen vacancies of the activated FeNi cathode after 20 recycles. The generation of oxygen vacancies were probably because under cathodic reactions, the surface H species may have infused into the lattice of the FeNi oxide layer and thus leads to segmentation of Fe—O or Ni—O bonds [39]. As a result, Fig. S10c shows that the NO_3^- concentrations declined at a slightly faster rate in the first

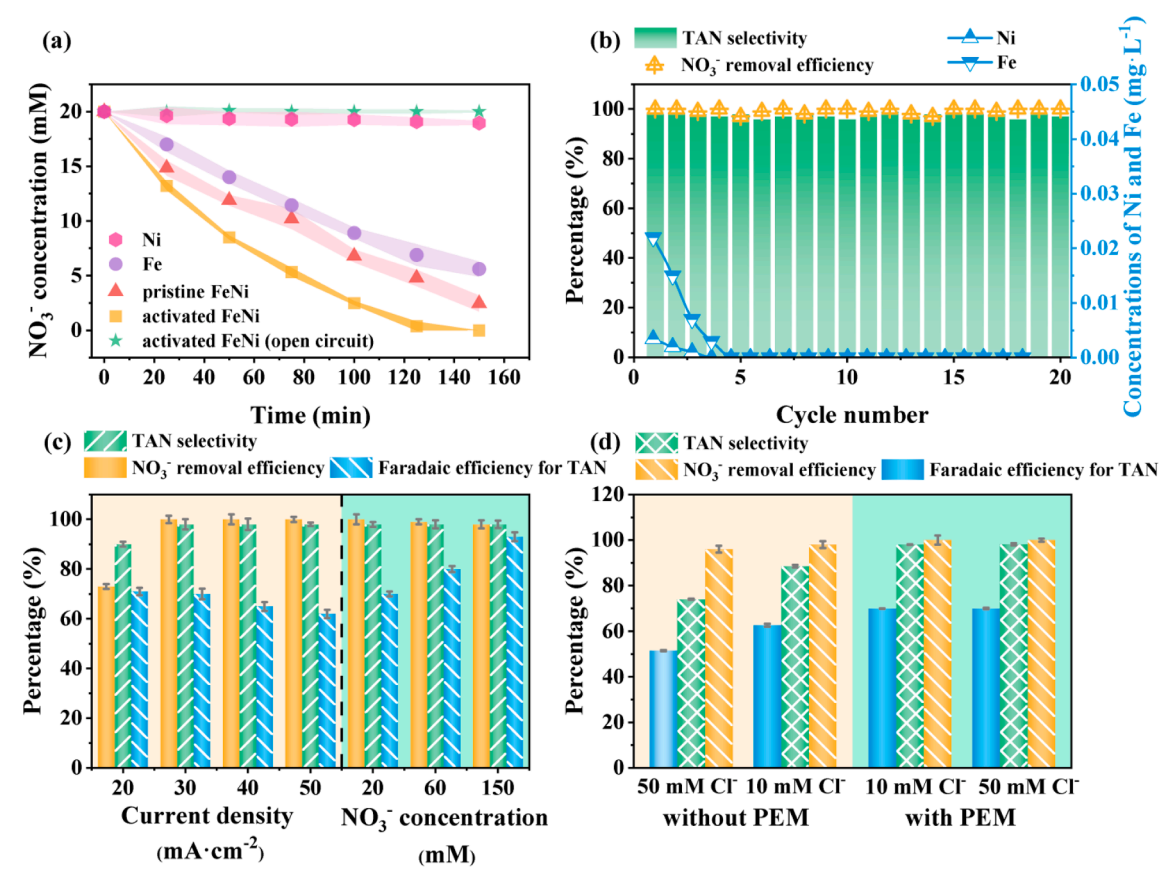


Fig. 4. (a) The comparison of NO_3^- reduction efficiency in various systems. (b) The NO_3^- removal efficiency, TAN selectivity, and the concentrations of the leached Fe and Ni ions over the 20 cycles. (c) the NO_3^- removal, TAN selectivity, and Faradaic efficiency for TAN at different current density and initial NO_3^- concentrations. (d) The TAN selectivity, Faradaic efficiency for TAN, and NO_3^- removal efficiency at different Cl $^-$ concentrations without/with incorporation of PEM between the anode and cathode. Major experimental conditions: cathode: activated FeNi, flow mode: flow-through, flow rate: 100 mL·min $^{-1}$, cathodic current density: 30 mA·cm $^{-2}$, initial NO_3^- concentration: 20 mM, pH \sim 7.0, and Cl $^-$: 10 mM.

cycle than in the twentieth cycle. The pseudo-first-order rate constant slightly increased from 1.849×10^{-2} to 2.134×10^{-2} min⁻¹, which suggests that the oxygen vacancies could facilitate the breakage of the O—N bond in electrochemical NO_3^- reduction [40].

Fig. 4c compares the Faradaic efficiency for TAN, NO_3^- removal efficiency, and TAN selectivity under different current densities and initial NO_3^- concentrations. Fig. S11 shows the detailed experimental results of the various nitrogen species concentrations. When the current density increased from 20 to 50 mA·cm $^{-2}$, the NO_3^- removal efficiency gradually increased from 73 % to 100 % within 2.5 h, with the increased NO_3^- removal rate from 246 to 560 g-N·m $^{-2}$ ·d $^{-1}$ and the increased TAN selectivity from 90 % to 98 %. However, a high current density results in a high cathodic potential (Table S3) that may trigger hydrogen evolution reactions (HER) and reduce the Faradaic efficiency for TAN from 71 % to 62 %. Thus, a cathodic current density of 30 mA·cm $^{-2}$ was consistently employed unless indicated otherwise.

Increasing the initial available NO_3^- concentration could improve the cathodic reduction of NO_3^- and inhibit HER [4]. Fig. 4c shows that when the initial NO_3^- concentration increased from 20 to 150 mM, the NO_3^- removal rate slightly increased from 336 to 444 g-N·m⁻²·d⁻¹ with minor changes in TAN selectivity and NO_3^- removal efficiency. However, the Faradaic efficiency for TAN significantly increased from 70 % to 93 %. Table S3 indicates that the cell voltage decreased with the increasing NO_3^- concentration (e.g., from 4.0 V at 20 mM NO_3^- to 3.2 V at 150 mM NO_3^-) at fixed electrolyte conductivity of 2.9 S·m⁻¹, suggesting that a higher energy utilization efficiency for NO_3^- reduction as shown in Fig. 5c. The internal potential losses, transport losses across the proton exchange membrane (PEM) separating cathode and anode chamber (E_{transfer}), ionic potential losses (E_{ionic}) were also analyzed. From Eqs.

(S27) and (S28), we calculate that the potential loss was 6.3×10^{-1} V, indicating that the potential loss was very small in this system.

Due to the prevalence of chloride ions in wastewater, oxidant species such as hypochlorite anions (HOCl) (Eqs. (S29) and (S30)) could also be simultaneously produced at the Ti/IrO2-RuO2 anode and may oxidize those intermediates such as NO₂ and NH₄ (Eqs. (S31)-(S33)) [41], and HOCl reacts also on NH₃ to form chloramines (Eqs. (S34)-(S37)) [8], which compromises the accumulation of NH₄ in the electrolyte. As illustrated in Fig. 4d, the Faradic efficiency for TAN and TAN selectivity all decreased as the ${\rm Cl}^-$ concentration increased from 10 to 50 mM when no PEM was used to separate the cathodic and anodic chambers. The NO₃ removal efficiency was barely affected by the presence of PEM or the Cl⁻ concentration. Conversely, when the PEM was incorporated, the transport of Cl⁻ from the cathode chamber into the anodic chamber was prevented and thus the anodic oxidation of Cl⁻ into OCl⁻ was avoided. As a result, the Faradic efficiency for TAN, TAN selectivity, and NO₃ removal efficiency were all increased to 70 %, 98 %, and 100 %, respectively, even when the Cl⁻ concentration was as high as 50 mM.

3.4. Evaluation of NO₃ to ammonia and conversion into (NH₄)₂SO₄

Fig. S12 shows the bulk anolyte pH rapidly dropped below 2.0 at a current density of 30 mA·cm $^{-2}$, while the bulk catholyte pH increased to>12.0, which improved the conversion of NH $_4^+$ to NH $_3$ and the NH $_3$ stripping since nearly 100 % of NH $_4^+$ will be converted to gaseous NH $_3$ at pH 12.0 according to Eq. (S38). The NH $_3$ in the catholyte was extracted or stripped by the hydrophobic polypropylene hollow fiber membrane that rejected water or ionic species. This membrane stripping is driven by the NH $_3$ partial pressure difference between the catholyte and the

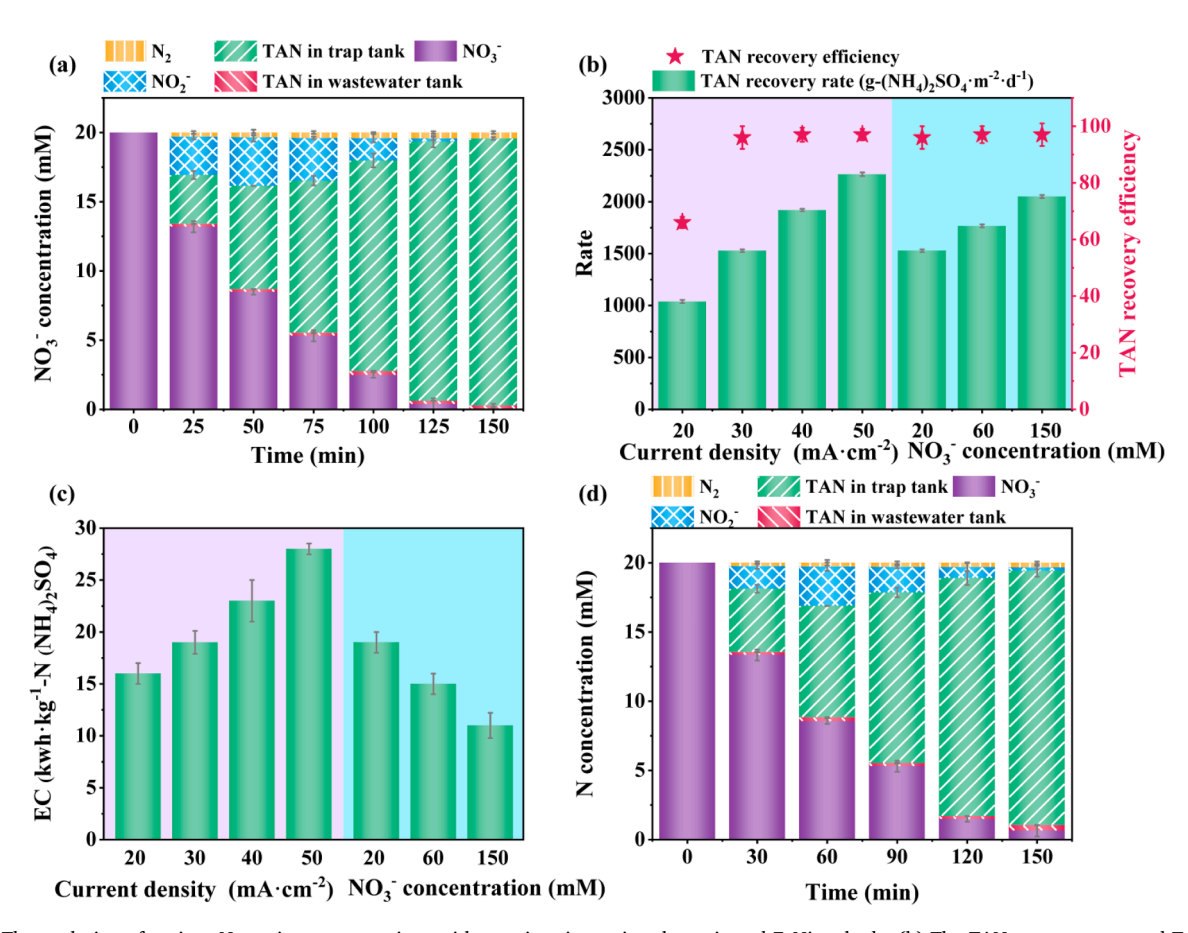


Fig. 5. (a) The evolution of various N species concentrations with reaction time using the activated FeNi cathode. (b) The TAN recovery rate and TAN recovery efficiency at different current density and initial NO_3^- concentration. (c) Energy consumption at different current density and initial NO_3^- concentration. (d) The evolution of various N species concentrations over time when recovering TAN from real wastewater. Major experimental conditions: flow rate: $100 \text{ mL} \cdot \text{min}^{-1}$, cathodic current density: $30 \text{ mA} \cdot \text{cm}^{-2}$, initial NO_3^- concentration: 20 mM, pH ~ 7.0 , and Cl $^-$: 10 mM.

acidic anolyte. According to the Henry's law in Eq. (S39), the NH $_3$ partial pressure outside the hollow fiber membrane is nearly zero, whereas the NH $_3$ partial pressure in the catholyte inside the hollow fiber membrane is 6 Pa, which thus drove the NH $_3$ transfer across the fiber membrane. Fig. 5a shows that at 30 mA·cm $^{-2}$, nearly 100 % NO $_3$ was progressively removed with reaction time, and almost 100 % of TAN was spontaneously extracted into the trap tank in the form of (NH $_4$) $_2$ SO $_4$ without significant accumulation in the rejected wastewater that contained only 0.3 mM NH $_4$. Similar to the above findings in Fig. S11, some NO $_2$ evolved but after 125 min they were not detected.

Fig. 5b further confirm that the TAN recovery efficiency and recovery rate were both increased from 66~% to 97~% and from 1039 to $2264~g\text{-}(NH_4)_2SO_4\text{·m}^{-2}\text{·d}^{-1}$ when increasing the current density (20–50 mA·cm⁻²), which also increased the specific energy consumption from $16~to~28~k\text{Wh}\cdot\text{kg}^{-1}\text{-}((NH_4)_2SO_4)$. Besides, when the initial NO_3^- concentration increased from 20~to~150~mM, the TAN recovery rate increased from $1529~to~2050~g\text{-}(NH_4)_2SO_4\text{·m}^{-2}\text{·d}^{-1}$, while the equilibrium TAN recovery efficiency of 97~% was not affected but the reaction time per cycle was increased to remove the increased NO_3^- content in wastewater. It is important to note that the NH_3 stripping rate (approximately $435~g\text{-N·m}^{-2}\text{·d}^{-1}$) nearly matched the electrolytic NO_3^- reduction rate ($444~g\text{-N·m}^{-2}\text{·d}^{-1}$) at NO_3^- concentration of 150~mM. The synchronized NH_3 production and extraction could effectively prevent the gaseous product accumulation on the cathode and reduce the electrolysis reaction time or extraction time as we reported previously [16].

Fig. 5c evaluated the specific energy consumption (EC) as the NO $_3^-$ concentration or the applied current density changed. The energy consumption decreased significantly from 19 to 11 kWh·kg $^{-1}$ -((NH $_4$)₂SO $_4$) as the NO $_3^-$ concentration increased from 20 to 150 mM at 30 mA·cm $^{-2}$, owing to the increased the Faradic efficiency for TAN and the reduced applied voltage. Obviously, increasing the current density led to greater energy consumption when using the same NO $_3^-$ concentration of 20 mM. It is important to note that the acidic anolyte (a mixture of Na $_2$ SO $_4$ and H $_2$ SO $_4$) could be reused with reproducible performances of NH $_3$ abstraction. Fig. S13 shows that the TAN concentrations in the acidic anolyte increased to 76 mM proportionally after four cycles without

replacing or refilling the Na_2SO_4 anolyte. The TAN recovery efficiency could still maintain at 95 % even after the fourth cycle, indicating that the H^+ concentration in the anolyte could be reproduced via anodic oxidation and no significant loss of Na^+ or SO_4^{2-} in NH_3 extraction or electrode reactions.

To evaluate the nitrate conversion of real wastewater using this continuous flow-through electrolysis cell, the NO $_3$ bearing wastewater was collected from Shandong Keyuan Pharmaceutical Co., Ltd. This real wastewater contained $280 \pm 8 \text{ mg} \cdot \text{L}^{-1} \text{ NO}_3$, $67 \pm 4 \text{ mg} \cdot \text{L}^{-1} \text{ Br}^-$, $240 \pm 11 \text{ mg} \cdot \text{L}^{-1} \text{Cl}^-$, $9650 \pm 46 \text{ mg} \cdot \text{L}^{-1} \text{ SO}_4^2$ -, $4657 \pm 25 \text{ mg} \cdot \text{L}^{-1} \text{Na}^+$, $3524 \pm 24 \text{ mg} \cdot \text{L}^{-1} \text{ K}^+$, and COD of $170 \pm 4 \text{ mg} \cdot \text{L}^{-1}$ with a solution pH 7.8 ± 0.5 . Fig. 5d shows the NO $_3$ removal efficiency, the TAN selectivity, Faradic efficiency for TAN, and TAN recovery efficiency that are comparable to those obtained with synthetic wastewater in Fig. 5a. The NO $_3$ removal rate and the NH $_3$ recovery rate reached $325 \text{ g-N} \cdot \text{m}^{-2} \cdot \text{d}^{-1}$ and $1500 \text{ g-} (\text{NH}_4)_2 \text{SO}_4 \cdot \text{m}^{-2} \cdot \text{d}^{-1}$. Notably, COD, Br $_7$, Cl $_7$, and K $_7$ were efficiently separated by the hydrophobic hollow fiber membrane (Table S4).

3.5. Mechanism analysis of electrocatalytic nitrate reduction to ammonia

3.5.1. Electron transfer and rate-limiting reaction analysis

 NO_3^- reduction to ammonia involves multi-electron-transfer processes to change nitrogen valence from +5 to -3. According to previous studies [41,42], the direct reduction mediated by electron transfer and/or the indirect reduction driven by surface-adsorbed hydrogen atoms (H*) could be responsible for the electrochemical NO_3^- reduction. To verify this speculation, tertiary butanol (t-BuOH) was employed to scavenge H* with the production of inert 2-methyl-2-propanol radicals [43]. Our results in Fig. 6a indicate that the NO_3^- removal rate was barely affected by the addition of t-BuOH at various t-BuOH: NO_3^- molar ratios. Thus, direct electron transfer should be a dominant mechanism for the electrolytic NO_3^- reduction.

The direct charge transfer often occurs through an inner sphere process and therefore requires direct interactions of the reactants (e.g., NO_3^-) with the charges on the catalytic sites [44]. To analyze this charge transfer process, we computed the charge distribution in Fig. 6b that

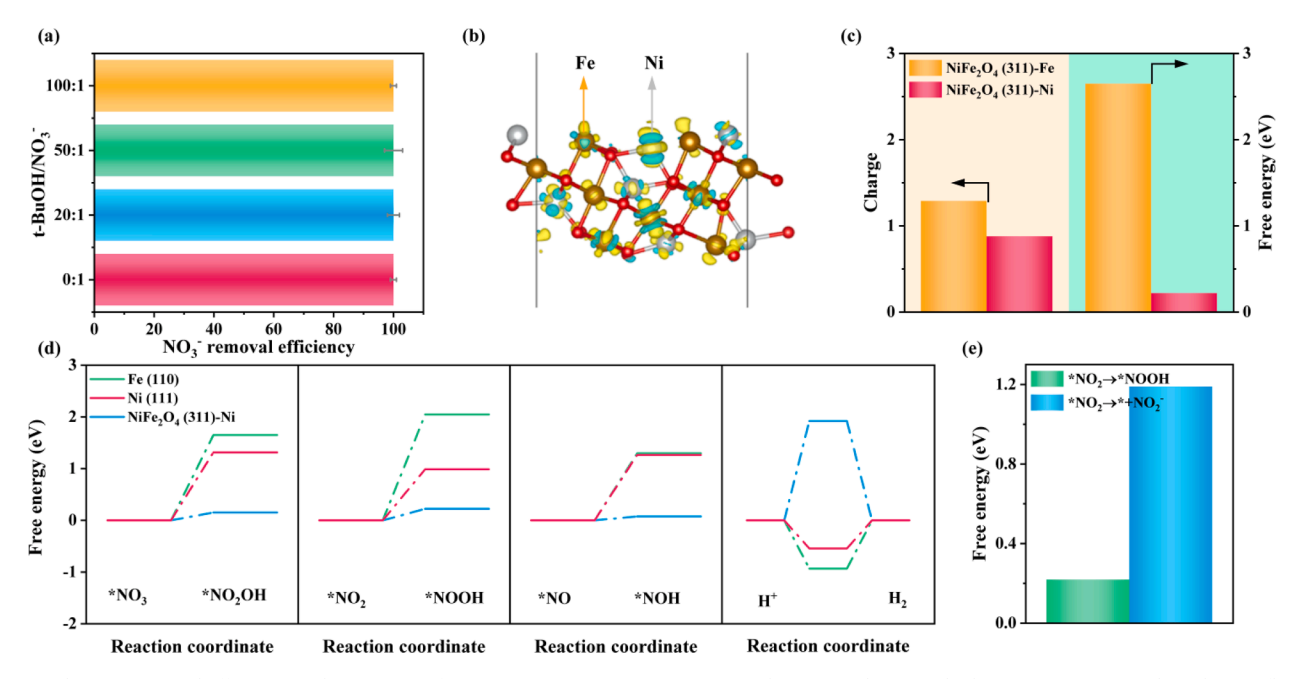


Fig. 6. (a) The NO_3^- removal efficiency in the presence of various t-BuOH concentrations using the activated FeNi cathode. Major experimental conditions: flow rate: $100 \text{ mL} \cdot \text{min}^{-1}$, cathodic current density: $30 \text{ mA} \cdot \text{cm}^{-2}$, initial NO_3^- concentration: 20 mM, pH ~ 7.0 , and Cl $^-$: 10 mM. (b) Electron distribution of extra electrons at the activated FeNi cathode, where electron depletion and accumulation are represented in blue and yellow, respectively. (c) Net charge distribution on NiFe $_2O_4$ (3 1 1)-Fe and NiFe $_2O_4$ (3 1 1)-Ni sites and the changes in Gibbs free energies of the NO_3^- adsorption on NiFe $_2O_4$ (3 1 1)-Fe and NiFe $_2O_4$ (3 1 1)-Ni sites. (d) The changes in Gibbs free energies of *NO $_3$ -to-*NO $_2O_4$, *NO $_2$ -to-*NOOH, *NO-to-*NOH, and H $^+ \to H_2$ reactions on NiFe $_2O_4$ (3 1 1)-Ni, Ni (1 1 1), and Fe (1 1 0) sites. (e) The changes in Gibbs free energies of the *NO $_2 \to *NOOH$ and *NO $_2 \to *+NO_2^-$ steps on NiFe $_2O_4$ (3 1 1)-Ni.

illustrates that the extra electrons (as indicated by yellow zones) are located on Fe and Ni sites at the NiFe $_2O_4$ (3 1 1). Fig. 6c further shows the net charge at the NiFe $_2O_4$ (3 1 1)-Ni sites is lower than that at the NiFe $_2O_4$ (3 1 1)-Fe sites, suggesting more valence electron is available on Ni sites. A relatively low adsorption energy (0.2 eV) for NO $_3^-$ occurred on the NiFe $_2O_4$ (3 1 1)-Ni site compared with the high adsorption energy (2.6 eV) on NiFe $_2O_4$ (3 1 1)-Fe site, which suggests that the NiFe $_2O_4$ (3 1 1)-Ni sites may be more favorable for the electrocatalytic NO $_3^-$ reduction. At the same time, NiFe $_2O_4$ (3 1 1)-Fe (0.8 eV) site is easier to adsorb H* than Ni (1.9 eV) site, which provides H* close to the surface for Ni site, so it promotes nitrate reduction (Fig. S14).

To determine the rate-determining steps of nitrate reduction reactions, the changes in Gibbs free energy (ΔG) of several key intermediate reactions (e.g., *NO₃-to-*HNO₃, *NO₂-to-*NOOH, and *NO-to-*NOH) have been calculated according to the reported DFT method [45,46]. Fig. 6d show the ΔG values of *NO₃-to-*HNO₃ (0.15 eV), *NO₂-to-*NOOH (0.22 eV), and *NO-to-*NOH (0.08 eV) on the NiFe₂O₄ (3 1 1)-Ni sites were lower than those on Fe (1 1 0) and Ni (1 1 1), which means those intermediate reactions tend to have lower energy barriers on the NiFe₂O₄ (3 1 1)-Ni sites. Moreover, the calculated ΔG of HER on the NiFe₂O₄ (3 1 1)-Ni sites (1.9 eV) showed a higher energy barrier than those on Fe (1 1 0) (-0.93 eV) and Ni (1 1 1) (-0.54 eV), suggesting that NiFe₂O₄ (3 1 1)-Ni was unfavorable for HER, which supports the LSV analysis in Fig. 3a. Thus, the activated FeNi cathode shows the superior intrinsic activity toward NO₃ reduction compared with pure Fe and Ni.

3.5.2. Selectivity for ammonia production

To confirm the high selectivity and specificity of the NiFe₂O₄ (3 1 1)-Ni site toward ammonia production over nitrogen production, we calculated the Gibbs free energies of two key intermediate reactions for ammonia and nitrogen respectively, *NO₂ \rightarrow *NOOH and *NO₂ \rightarrow * + NO $_2^-$ [47]. For example, during electrocatalytic nitrate reduction, N₂ is often produced through the reactions of NO $_2^-$ and other N intermediates (e.g., *NO), whereas NH₃ is formed in a number of series reaction Eq. (S10-S26) mainly involving *NOOH. Our results in Fig. 6e show that the Gibbs free energy of *NO $_2$ \rightarrow * + NO $_2^-$ is 1.19 eV and is more positive than that 0.22 eV of *NO $_2$ \rightarrow *NOOH. Thus, the N₂ production is unfavorable relatively to the production of ammonia.

3.6. Analysis of energy Consumption, economic viability and environmental benefits

The presented activated FeNi alloy cathode in this study exhibited efficient NO₃ reduction toward ammonia with a NO₃ removal rate of 99 %, a TAN selectivity of 98 % and a Faradic efficiency of 93 %, which outcompetes many other cathode materials as summarized in Table S5. In addition, the TAN recovery efficiency of 97 % could be achieved at in the trap tank with the use of hollow fiber membranes. But in this system, there will be the problems of membrane fouling regardless of proton exchange membrane and hollow fiber membranes. To solve the problem of membrane fouling contamination, some pretreatment processes such as coagulation, adsorption and oxidation are required to combine with the concurrent electrocatalysis and membrane extraction to prevent it. Table S6 compares the ammonia recovery efficiencies of different NH₃ recovery systems, which achieved 10 %-80 %. Besides, the energy consumption for NH₃ recovery is 11 kWh·kg⁻¹-(NH₄)₂SO₄ when the NO₃ concentration was 150 mM, which is lower than many other systems and demonstrates high economic viability [48]. This is mainly attributed to the high activity of the prepared catalyst toward the reduction of NO₃⁻ to NH₄⁺ side hydrogen evolution reaction, the enhanced mass transport of nitrate toward the active sites of FeNi foam cathode and the rapid equilibrium between NO3-and NO3 solution [49]. For instance, electrochemically selective NH3 extraction, capacitive membrane stripping, and capacitive deionization-like electrochemical reactor rendered high energy consumptions at 19-57 kWh·kg⁻¹-(NH₄)₂SO₄. Moreover, those above processes usually

consume external acid or base to adjust pHs, which is not required for this continuous flow-through electrolysis process. The continuous flowthrough electrolysis system also exhibits some additional economic and environmental benefits. For example, the industrial Haber-Bosch process for ammonia synthesis uses large amounts of fossil fuels and releases around 465×10^9 kg CO₂ each year globally [50]. To relieve this environmental and energy burden, a shift of nitrogen removal from the wastewater to nitrogen recovery is critical. It is worth noting that the present electrolysis system can be driven by renewable energy sources (e.g., wind power or hydropower) with reduced or neutral CO₂ emission. Moreover, the high pHs in the treated water (>12.5) could facilitate the water hardness reduction (Ca²⁺ and Mg²⁺) and production of phosphorus containing fertilizer (e.g., struvite or calcium phosphate). Finally, in addition to (NH₄)₂SO₄, the produced NH₃ could be recovered in many other forms (e.g., ammonium phosphate and ammonium nitrate) by changing the anolytes.

4. Conclusion

Although electrocatalytic ammonia synthesis from NO₃ in wastewater is an attractive concept, its practical implementation could be still hindered by the complex catalyst preparation, catalytic reaction, and synchronization with NH3 recovery. This study proved the feasibility of this continuous flow-through electrolysis cell with the porous activated FeNi cathode and hollow fiber membranes-based extraction for upcycling NO₃ into NH₄ fertilizer. The system achieved a TAN recovery efficiency of 97 % and a specific NH3 recovery rate of 2050 g- $(NH_4)_2SO_4 \cdot m^{-2} \cdot d^{-1}$. The experimental and DFT analysis both indicate that direct electron transfer was the main mechanism for the electrocatalytic NO₃ to ammonia reactions. The NiFe₂O₄ (3 1 1)-Ni site on the activated FeNi cathode was the main active site for the intermediate reactions (e.g., *NO3, *NO2, and *NO), because of the relatively low reaction barrier for the NO₃ reduction to ammonia and high specificity toward ammonia over N2 generation. Overall, this presented technology may have promising potentials to transform traditional biological nitrogen removal and industrial ammonia production and lead to sustainable synergies in resource recovery from wastewater.

CRediT authorship contribution statement

Ning Shi: Validation, Writing – original draft. Jianan Gao: Validation, Writing – original draft. Kai Li: Supervision. Yifan Li: . Wen Zhang: Writing – review & editing. Qipeng Yang: Resources. Bo Jiang: Conceptualization, Writing – review & editing.

Declaration of Competing Interest

The authors declare that they have no known competing financial interests or personal relationships that could have appeared to influence the work reported in this paper.

Data availability

The data that has been used is confidential.

Acknowledgements

This work is financially supported by the Natural Science Foundation of Shandong Province (Award number: ZR2021MB003, ZR2021QB205, ZR2022QB114) and partially supported by the NSF-BSF Grant (Award number: 2215387).

Appendix A. Supplementary data

Supplementary data to this article can be found online at https://doi.org/10.1016/j.cej.2022.140959.

References

- [1] J.G. Chen, R.M. Crooks, L.C. Seefeldt, K.L. Bren, R.M. Bullock, M.Y. Darensbourg, P.L. Holland, B. Hoffman, M.J. Janik, A.K. Jones, Beyond fossil fuel-driven nitrogen transformations, Science 360 (6391) (2018) eaar6611, https://doi.org/ 10.1126/science.aar6611.
- [2] J.M. McEnaney, S.J. Blair, A.C. Nielander, J.A. Schwalbe, D.M. Koshy, M. Cargnello, T.F. Jaramillo, Electrolyte engineering for efficient electrochemical nitrate reduction to ammonia on a titanium electrode, ACS Sustain. Chem. Eng. 8 (7) (2020) 2672–2681, https://doi.org/10.1021/acssuschemeng.9b05983.
- [3] H. Hirakawa, M. Hashimoto, Y. Shiraishi, T. Hirai, Selective nitrate-to-ammonia transformation on surface defects of titanium dioxide photocatalysts, ACS Catal. 7 (5) (2017) 3713–3720. https://doi.org/10.1021/acscatal.7b00611.
- [4] W. Zheng, L. Zhu, Z. Yan, Z. Lin, Z. Lei, Y. Zhang, H. Xu, Z. Dang, C. Wei, C. Feng, Self-activated Ni cathode for electrocatalytic nitrate reduction to ammonia: from fundamentals to scale-up for treatment of industrial wastewater, Environ. Sci. Technol. 55 (19) (2021) 13231–13243, https://doi.org/10.1021/acs.est.1c02278.
- [5] H. Xu, Y. Ma, J. Chen, W.-X. Zhang, J. Yang, Electrocatalytic reduction of nitrate–a step towards a sustainable nitrogen cycle, Chem. Soc. Rev. 51 (2022) 2710–2758, https://doi.org/10.1039/D1CS00857A.
- [6] Y. Wang, A. Xu, Z. Wang, L. Huang, J. Li, F. Li, J. Wicks, M. Luo, D.-H. Nam, C.-S. Tan, Y.u. Ding, J. Wu, Y. Lum, C.-T. Dinh, D. Sinton, G. Zheng, E.H. Sargent, Enhanced nitrate-to-ammonia activity on copper-nickel alloys via tuning of intermediate adsorption, J. Am. Chem. Soc. 142 (12) (2020) 5702–5708.
 [7] C. Wang, Y. Zhang, H. Luo, H. Zhang, W. Li, W.-X. Zhang, J. Yang, Iron-based
- [7] C. Wang, Y. Zhang, H. Luo, H. Zhang, W. Li, W.-X. Zhang, J. Yang, Iron-based nanocatalysts for electrochemical nitrate reduction, Small Methods 6 (10) (2022) 2200790.
- [8] S. Garcia-Segura, M. Lanzarini-Lopes, K. Hristovski, P. Westerhoff, Electrocatalytic reduction of nitrate: Fundamentals to full-scale water treatment applications, Appl. Catal. B 236 (2018) 546–568, https://doi.org/10.1016/j.apcatb.2018.05.041.
- [9] H. Wu, C. Vaneeckhaute, Nutrient recovery from wastewater: A review on the integrated Physicochemical technologies of ammonia stripping, adsorption and struvite precipitation, Chem. Eng. J. 433 (2022) 133664.
- [10] F. Ferrari, M. Pijuan, S. Molenaar, N. Duinslaeger, T. Sleutels, P. Kuntke, J. Radjenovic, Ammonia recovery from anaerobic digester centrate using onsite pilot scale bipolar membrane electrodialysis coupled to membrane stripping, Water Res. 218 (2022), 118504, https://doi.org/10.1016/j.watres.2022.118504.
- [11] P. Kuntke, M. Rodríguez Arredondo, L. Widyakristi, A. Ter Heijne, T.H. Sleutels, H. V. Hamelers, C.J. Buisman, Hydrogen gas recycling for energy efficient ammonia recovery in electrochemical systems, Environ. Sci. Technol. 51 (5) (2017) 3110–3116, https://doi.org/10.1021/acs.est.6b06097.
- [12] L. Hu, J. Yu, H. Luo, H. Wang, P. Xu, Y. Zhang, Simultaneous recovery of ammonium, potassium and magnesium from produced water by struvite precipitation, Chem. Eng. J. 382 (2020) 123001.
- [13] L. Fang, S. Wang, C. Song, S. Lu, X. Yang, X. Qi, H. Liu, Boosting nitrate electroreduction to ammonia via in situ generated stacking faults in oxide-derived copper, Chem. Eng. J. 446 (2022) 137341.
- [14] W. Fu, Z. Hu, Y. Zheng, P. Su, Q. Zhang, Y. Jiao, M. Zhou, Tuning mobility of intermediate and electron transfer to enhance electrochemical reduction of nitrate to ammonia on $\text{Cu}_2\text{O}/\text{Cu}$ interface, Chem. Eng. J. 433 (2022), 133680, https://doi.org/10.1016/j.cej.2021.133680.
- [15] F. Lei, W. Xu, J. Yu, K. Li, J. Xie, P. Hao, G. Cui, B. Tang, Electrochemical synthesis of ammonia by nitrate reduction on indium incorporated in sulfur doped graphene, Chem. Eng. J. 426 (2021), 131317, https://doi.org/10.1016/j.cej.2021.131317.
- [16] J. Gao, N. Shi, Y. Li, B. Jiang, T. Marhaba, W. Zhang, Electrocatalytic upcycling of nitrate wastewater into an ammonia fertilizer via an electrified membrane, Environ. Sci. Technol. 56 (16) (2022) 11602–11613, https://doi.org/10.1021/acs. est.1c08442.
- [17] J. Zhang, Y. Jiang, Y. Wang, C. Yu, J. Cui, J. Wu, X. Shu, Y. Qin, J. Sun, J. Yan, H. Zheng, Y. Zhang, Y. Wu, Ultrathin carbon coated mesoporous Ni-NiFe₂O₄ nanosheet arrays for efficient overall water splitting, Electrochim. Acta 321 (2019) 134652
- [18] Z. Xing, L. Hu, D.S. Ripatti, X. Hu, X. Feng, Enhancing carbon dioxide gas-diffusion electrolysis by creating a hydrophobic catalyst microenvironment, Nat. Commun. 12 (1) (2021) 1–11, https://doi.org/10.1038/s41467-020-20397-5.
- [19] Y. Zhao, N. Deng, Z. Fan, Z.-T. Hu, L. Fan, J. Zhou, X. Huang, On-site H₂O₂ electrogeneration process combined with ultraviolet: A promising approach for odorous compounds purification in drinking water system, Chem. Eng. J. 430 (2022) 123220
- [20] Z. Liu, G. Zhang, H. Lan, H. Liu, J. Qu, Optimization of a Hierarchical Porous-Structured Reactor to Mitigate Mass Transport Limitations for Efficient Electrocatalytic Ammonia Oxidation through a Three-Electron-Transfer Pathway, Environ. Sci. Technol. 55 (18) (2021) 12596–12606, https://doi.org/10.1021/acs. est.1c02825.
- [21] J. Zhou, F. Pan, Q. Yao, Y. Zhu, H. Ma, J. Niu, J. Xie, Achieving efficient and stable electrochemical nitrate removal by in-situ reconstruction of Cu₂O/Cu electroactive nanocatalysts on Cu foam, Appl. Catal. B 317 (2022) 121811.
- [22] J. Gao, B. Jiang, C. Ni, Y. Qi, X. Bi, Enhanced reduction of nitrate by noble metal-free electrocatalysis on P doped three-dimensional Co₃O₄ cathode: Mechanism exploration from both experimental and DFT studies, Chem. Eng. J. 382 (2020), 123034, https://doi.org/10.1016/j.cej.2019.123034.
- [23] S. Maheshwari, G. Rostamikia, M.J. Janik, Elementary kinetics of nitrogen electroreduction on Fe surfaces, J. Chem. Phys. 150 (4) (2019), 041708, https://doi.org/10.1063/1.5048036.
- [24] C. Lu, X. Lu, K. Yang, H. Song, S. Zhang, A. Li, Cu, Ni and multi-walled carbonnanotube-modified graphite felt electrode for nitrate electroreduction in water,

- J. Mater. Sci. 56 (12) (2021) 7357–7371, https://doi.org/10.1007/s10853-020-05764.2
- [25] D. Li, H. Liu, L. Feng, A review on advanced FeNi-based catalysts for water splitting reaction, Energy Fuels 34 (11) (2020) 13491–13522, https://doi.org/10.1021/acs. energyfuels.0c03084.
- [26] G. Gebreslassie, P. Bharali, U. Chandra, A. Sergawie, P.K. Baruah, M.R. Das, E. Alemayehu, Hydrothermal synthesis of g-C₃N₄/NiFe₂O₄ nanocomposite and its enhanced photocatalytic activity, Appl Organomet Chem 33 (8) (2019) e5002.
- [27] M. Chen, S. Lu, X.Z. Fu, J.L. Luo, Core-Shell structured NiFeSn@NiFe (Oxy) Hydroxide nanospheres from an electrochemical strategy for electrocatalytic oxygen evolution reaction, Adv. Sci. 7 (10) (2020) 1903777, https://doi.org/ 10.1002/advs.201903777.
- [28] Y. Gan, M. Cui, X. Dai, Y. Ye, F. Nie, Z. Ren, X. Yin, B. Wu, Y. Cao, R. Cai, X. Zhang, Mn-doping induced electronic modulation and rich oxygen vacancies on vertically grown NiFe₂O₄ nanosheet array for synergistically triggering oxygen evolution reaction. Nano Res. 15 (5) (2022) 3940–3945.
- [29] M. Salavati-Niasari, F. Davar, T. Mahmoudi, A simple route to synthesize nanocrystalline nickel ferrite (NiFe₂O₄) in the presence of octanoic acid as a surfactant, Polyhedron 28 (8) (2009) 1455–1458, https://doi.org/10.1016/j. poly.2009.03.020.
- [30] L.-H. Yao, J.-G. Zhao, Q.-L. Pan, X.-Y. Li, B.-Y. Xing, S. Jiang, J. Song, M.-J. Pang, Tailoring NiO@NiFe₂O₄/CNTs triphase hybrids towards high-performance anode for lithium-ion batteries, J. Alloys Compd. 912 (2022), 165209, https://doi.org/ 10.1016/j.jallcom.2022.165209.
- [31] T. Yamashita, P. Hayes, Analysis of XPS spectra of Fe²⁺ and Fe³⁺ ions in oxide materials, Appl. Surf. Sci. 254 (8) (2008) 2441–2449, https://doi.org/10.1016/j. apsusc.2007.09.063.
- [32] Z. Huang, N. Gao, Y. Lin, G. Wei, K. Zhao, A. Zheng, Z. Zhao, H. Yuan, H. Li, Exploring the migration and transformation of lattice oxygen during chemical looping with NiFe₂O₄ oxygen carrier, Chem. Eng. J. 429 (2022), 132064, https://doi.org/10.1016/j.cej.2021.132064.
- [33] T. Wu, S. Sun, J. Song, S. Xi, Y. Du, B.o. Chen, W.A. Sasangka, H. Liao, C.L. Gan, G. G. Scherer, L. Zeng, H. Wang, H. Li, A. Grimaud, Z.J. Xu, Scherer, Iron-facilitated dynamic active-site generation on spinel CoAl₂O₄ with self-termination of surface reconstruction for water oxidation, Nat Catal 2 (9) (2019) 763–772.
- [34] H. Li, S. Chen, X. Jia, B. Xu, H. Lin, H. Yang, L. Song, X. Wang, Amorphous nickel-cobalt complexes hybridized with 1T-phase molybdenum disulfide via hydrazine-induced phase transformation for water splitting, Nat. Commun. 8 (1) (2017) 1–11, https://doi.org/10.1038/ncomms15377.
- [35] Y.i. Li, W. Shan, M.J. Zachman, M. Wang, S. Hwang, H. Tabassum, J. Yang, X. Yang, S. Karakalos, Z. Feng, G. Wang, G. Wu, Atomically Dispersed Dual-Metal Site Catalysts for Enhanced CO₂ Reduction: Mechanistic Insight into Active Site Structures, Angew. Chem. Int. Ed. 61 (28) (2022) e202205632, https://doi.org/ 10.1002/anie.202205632.
- [36] C.-F. Li, L.-J. Xie, J.-W. Zhao, L.-F. Gu, J.-Q. Wu, G.-R. Li, Interfacial Electronic Modulation by Fe₂O₃/NiFe-LDHs Heterostructures for Efficient Oxygen Evolution at High Current Density, Appl. Catal. B 306 (2022) 121097.
- [37] Q. Zhu, M. Hinkle, D.J. Kim, J.-H. Kim, Modular hydrogen peroxide electrosynthesis cell with anthraquinone-modified polyaniline electrocatalyst, ACS EST Engs. 1 (3) (2020) 446–455, https://doi.org/10.1021/acsestengg.0c00173.
- [38] J. Rui, N. Deng, Y. Zhao, C. Tao, J. Zhou, Z. Zhao, X. Huang, Activation of persulfate via Mn doped Mg/Al layered double hydroxide for effective degradation of organics: Insights from chemical and structural variability of catalyst, Chemosphere 302 (2022), 134849, https://doi.org/10.1016/j. chemosphere 2022 134849
- [39] X. Chen, T. Zhang, M. Kan, D. Song, J. Jia, Y. Zhao, X. Qian, Binderless and oxygen vacancies rich FeNi/graphitized mesoporous carbon/Ni foam for electrocatalytic reduction of nitrate, Environ. Sci. Technol. 54 (20) (2020) 13344–13353, https://doi.org/10.1021/acs.est.0c05631.
- [40] R. Jia, Y. Wang, C. Wang, Y. Ling, Y. Yu, B. Zhang, Boosting selective nitrate electroreduction to ammonium by constructing oxygen vacancies in TiO₂, ACS Catal. 10 (6) (2020) 3533–3540, https://doi.org/10.1021/acscatal.9b05260.
- [41] F. Yao, M. Jia, Q.i. Yang, F. Chen, Y.u. Zhong, S. Chen, L.i. He, Z. Pi, K. Hou, D. Wang, X. Li, Highly selective electrochemical nitrate reduction using copper phosphide self-supported copper foam electrode: performance, mechanism, and application, Water Res. 193 (2021) 116881.
- [42] J. Gao, B. Jiang, C. Ni, Y. Qi, Y. Zhang, N. Oturan, M.A. Oturan, Non-precious Co₂O₄-TiO₂/Ti cathode based electrocatalytic nitrate reduction: Preparation, performance and mechanism, Appl. Catal. B 254 (2019) 391–402, https://doi.org/10.1016/j.apcatb.2019.05.016.
- [43] J. Zhang, G. Zhang, H. Lan, J. Qu, H. Liu, Synergetic Hydroxyl Radical Oxidation with Atomic Hydrogen Reduction Lowers the Organochlorine Conversion Barrier and Potentiates Effective Contaminant Mineralization, Environ. Sci. Technol. 55 (5) (2021) 3296–3304, https://doi.org/10.1021/acs.est.0c07271.
- [44] K. Flores, G.A. Cerrón-Calle, C. Valdes, A. Atrashkevich, A. Castillo, H. Morales, J. G. Parsons, S. Garcia-Segura, J.L. Gardea-Torresdey, Outlining Key Perspectives for the Advancement of Electrocatalytic Remediation of Nitrate from Polluted Waters, ACS EST Engs. 2 (5) (2022) 746–768, https://doi.org/10.1021/acsestengs.2c00052.
- [45] X. Fan, L. Xie, J. Liang, Y. Ren, L. Zhang, L. Yue, T. Li, Y. Luo, N.a. Li, B.o. Tang, Y. Liu, S. Gao, A.A. Alshehri, Q. Liu, Q. Kong, X. Sun, In situ grown Fe₃O₄ particle on stainless steel: A highly efficient electrocatalyst for nitrate reduction to ammonia, Nano Res. 15 (4) (2022) 3050–3055.
- [46] W.J. Sun, H.Q. Ji, L.X. Li, H.Y. Zhang, Z.K. Wang, J.H. He, J.M. Lu, Built-in Electric Field Triggered Interfacial Accumulation Effect for Efficient Nitrate Removal at

- Ultra-Low Concentration and Electroreduction to Ammonia, Angew. Chem. Int. Ed. 60 (42) (2021) 22933–22939, https://doi.org/10.1002/anie.202109785.
- [47] G.-F. Chen, Y. Yuan, H. Jiang, S.-Y. Ren, L.-X. Ding, L. Ma, T. Wu, J. Lu, H. Wang, Electrochemical reduction of nitrate to ammonia via direct eight-electron transfer using a copper–molecular solid catalyst, Nat Energy 5 (2020) 605–613, https://doi. org/10.1038/s41560-020-0654-1.
- [48] J. Gao, N. Shi, X. Guo, Y. Li, X. Bi, Y. Qi, J. Guan, B. Jiang, Electrochemically selective ammonia extraction from nitrate by coupling electron-and phase-transfer
- reactions at a three-phase interface, Environ. Sci. Technol. 55 (15) (2021) 10684–10694, https://doi.org/10.1021/acs.est.0c08552.
- [49] N.C. Antonels, R. Meijboom, Preparation of well-defined dendrimer Encapsulated ruthenium nanoparticles and their evaluation in the reduction of 4-nitrophenol according to the Langmuir-Hinshelwood approach, Langmuir 29 (44) (2013) 13433–13442.
- [50] S.-W. Tsai, D.V. Cuong, C.-H. Hou, Selective capture of ammonium ions from municipal wastewater treatment plant effluent with a nickel hexacyanoferrate electrode, Water Res. 221 (2022) 118786.